

# Numerical modelling of a mantle plume: the plume head–lithosphere interaction in the formation of an oceanic large igneous province

Elia d’Acremont\*, Sylvie Leroy, Evgenii B. Burov

*Laboratoire de Tectonique, CNRS, UMR 7072, Université Pierre et Marie Curie, Case 129, 4 Place Jussieu,  
75252 Paris Cedex 05, France*

Received 24 July 2002; received in revised form 30 October 2002; accepted 4 November 2002

## Abstract

The thermomechanical processes associated with formation of large igneous provinces (LIPs) remain poorly understood owing to fundamental difficulties in simulating plume–lithosphere interactions in current numerical models. These models, which aim to simulate the rise of mantle plume and the spread of plume head material, imply a mechanically over-simplified lithosphere and, commonly, a flat lithosphere (zero vertical displacement) as the upper boundary condition. We propose a new numerical model, derived from lithospheric-scale models. It has a high numerical resolution in the lithospheric domain and explicitly accounts for: (1) free upper surface boundary condition, (2) elastic–plastic–ductile lithospheric rheology, including surface faulting, and (3) vertical strength variations in the lithosphere. We study the final stages of plume ascent and we focus on surface and lithospheric evolution and intra-plate strain localisations. The experiments predict that the first surface elevation occurs in less than 0.2 Ma after plume initiation at 400 km depth. Variation of rheological parameters results in different surface elevations (500–2500 m), ascent (2–10 m/yr) and base plate strain rates ( $10^{-12}$ – $10^{-15}$  s $^{-1}$ ). Fast (0.2–0.3 m/yr) plume head flattening starts at the moment when the plume head reaches the base of the lithosphere. It leads to large-scale extension and deep normal faulting at the centre of the plateau, and to strong thermomechanical erosion at its base. The erosion is maximal not under the plume centre (as was predicted before), but in two large bordering zones. Our study locally is the igneous province of the Caribbean plate where the pre-existing (Farallon) lithosphere has been affected by the Galapagos hotspot activity that generated thermal perturbations and crustal thickening with two main episodes of volcanism and underplating.

© 2002 Elsevier Science B.V. All rights reserved.

*Keywords:* oceanic large igneous province; mantle plume; numerical model; lithospheric scale

## 1. Introduction

Mantle plumes are considered as the most probable explanation for hotspot tracks, and for the formation of the large igneous provinces (LIPs) [1–3]. Yet geophysical (i.e. seismological)

\* Corresponding author. Tel.: +33-1-44275256;

Fax: +33-1-44275085.

*E-mail addresses:* [elia.dacremont@lgs.jussieu.fr](mailto:elia.dacremont@lgs.jussieu.fr)  
(E. d’Acremont), [sylvie.leroy@lgs.jussieu.fr](mailto:sylvie.leroy@lgs.jussieu.fr) (S. Leroy),  
[evgenii.burov@lgs.jussieu.fr](mailto:evgenii.burov@lgs.jussieu.fr) (E.B. Burov).

methods allow only for quite scant and ambiguous images of plumes where they interact with continental lithosphere. For this reason, many indirect methods (theoretical, experimental and numerical modelling) are used to tackle this problem.

One of the first physical models consistent with field observations on flood basalts and hotspot tracks has been developed by Griffiths and Campbell [4]. According to some earlier laboratory experiments [5,6], a plume initiates as a Rayleigh–Taylor instability in a thermal boundary layer and rises through the mantle, forming a spherical head with a thinner tail connecting it to the source region. As the plume head arrives at the bottom of the lithosphere, it starts flattening. Flattening is conditioned by a number of factors: (1) decrease in buoyancy force near the surface; (2) vicinity of the upper surface [7]; (3) strong rheological contrast at the plume–lithosphere interface; (4) reaction of the resistant surface layer (lithosphere). In most analytical and in some numerical models, this process is studied using thin-layer approximation of the lubrication theory that considers thin channel flow, which is driven by pressure gradients due to body forces and conditioned by variable channel thickness and by normal loads acting on channel walls [5,7,8]. The mechanical reaction, e.g. flexure, of the channel walls is commonly ignored, although lithospheric-scale studies (e.g. [9,10]) show that this reaction may strongly influence the flow. Indeed, the plume head induces not only thermal weakening and shear at the bottom of the lithosphere, but also the observed large-scale flexure of the lithosphere [10]. Flexural stresses result in localised inelastic yielding, that is, an additional weakening of the lithosphere which is as important as thermal weakening ([11] and references therein). The above four factors result in lithospheric rifting or greatly enhance it. Far-field tectonic forces also cause or enhance rifting (e.g. [12,13]), so that either of the two end-member models of plume–lithosphere interaction, active or passive rifting, are possible, as well as their combinations [14,15].

### 1.1. Models of plume–lithosphere interaction and non-viscous rheology

Thermomechanical processes of plume–lithospheric interactions are not well studied in terms of lithospheric behaviour. Until recently, this problem was tackled using a purely hydrodynamic approach (e.g. [7,8,16–22]). Most models of plume ascent consider the lithosphere as a simple stagnant lid with a fixed surface and use different viscous or effective viscous rheological profiles for the whole mantle–lithosphere system. Instead, lithospheric-scale studies demonstrate that the lithosphere behaves as a elastic–brittle–ductile multi-layer, whose large-scale behaviour involves important flexural deformation. This system strongly differs from a viscous lid. Plume models based on viscous flow equations cannot handle non-viscous properties, which are only simulated using pseudoplasticity and pseudoelasticity (e.g. [16,19]), i.e. by ‘fake’ viscosity with damage law. This approach is justified for mantle-scale studies but it is not applicable in cases when lithospheric-scale deformation is also in focus (e.g. [23]). At the lithospheric scale, damage viscosity provides a poor approximation to Byerlee’s law of brittle rock failure [24], and high viscosity is not a good approximation to rheologies with a linear strain/stress dependence such as elasticity. Viscous rheology relates stress to strain rate, while brittle behaviour is strain rate-independent but pressure-dependent [23,24]. In particular, brittle shear zones and faults, which are important features of lithospheric deformation, are difficult to reproduce using a hydrodynamic approach.

### 1.2. Prediction of upper surface deformation

Most numerical models of plume–lithosphere interactions (e.g. [8]) do not handle the free upper surface boundary condition. Yet this condition is needed for reliable prediction of surface topography. Instead, the typically assumed upper boundary condition is a fixed (e.g. zero) vertical velocity or displacement. Surface deformation is thus only approximately estimated assuming that real surface uplift follows the neutral buoyancy level. This assumption means local isostasy and implies

zero lithospheric strength, i.e. no lithospheric flexure or localised deformation. It is also inherently incompatible with the high viscosity attributed to the stagnant lid. For example, the 110 Ma old lithosphere over the Hawaiian hotspot exhibits very large observable variations in flexural rigidity [25]. These variations occur at hotspot swell wavelengths and thus cannot be ignored.

To circumvent these limitations, some authors (e.g. [25]) used a combination of an analytical elastic bending solution for the lithosphere with a simplified viscous flow solution for the plume. This approach provides only a first-order approximation to lithosphere–plume head interaction, because, as was previously shown [11], lithospheric flexure involves strong inelastic weakening. Moreover, flexure is also only a part of lithospheric reaction to normal and shear loads, with the other part being attributed to extensional necking, faulting and various forms of tensional and compressional instabilities [26].

A number of authors [27] have also suggested that surface deformation over hotspots is controlled by compositional buoyancy associated with depleted mantle rock. This theory was contested by [28], who demonstrated that the sign of curvature of the observed topography and of the geoid will be opposite to that expected from the compositional buoyancy model.

### 1.3. Driving forces

Density anomaly with embeddings both drives plume ascent and controls forces applied at the base of the lithosphere. A simple approach to estimate the buoyancy force associated with the plume is to consider the density anomaly  $\Delta\rho$  due to thermal expansion of mantle/plume material (with initial density  $\rho_m$ ) induced by a temperature difference  $\Delta T$  (e.g. [29]):

$$\Delta\rho = \rho_m\alpha\Delta T \quad (1)$$

Most estimations point to  $\Delta T$  values of order 100–300°C, which result in  $\Delta\rho$  values of 10–30 kg/m<sup>3</sup>. These values are questioned because experimental data indicate strong variation of  $\alpha$  with temperature and pressure.  $\alpha$  first strongly increases and then decreases with growing depth–

temperature [30]. It is twice larger at 400°C at appropriate lithospheric pressure and still increases until the depth to the base of the lithosphere [31] (1300°C). Below this depth  $\alpha$  starts to decrease due to growing pressure, and becomes twice lower at 400–660 km. Eq. 1 thus appears to be only a first-order approximation. If the plume material is buoyant at 410 or 660 km, this may be due to higher than conventional  $\Delta T$  values or due to initial chemical density contrasts. The initial  $\Delta T$  may be as high as 500°C (C. Jaupart, personal communication, 2002). Mantle plumes originate from the lower mantle (below 660 km depth) and thus undergo phase transitions and chemical transformations on their way to the surface. It is therefore possible that chemical density contrast with the surrounding rock is as important as the thermally induced contrast.

### 1.4. Flood basalts and ascent rates. Benchmarking difficulties

Massive flood basalt eruptions result from partial melting of the plume head intruding into the lithosphere. These eruptions supposedly mark the initiation of hotspot tracks [32]. Many studies [4,7,20,28,33,34] have appeared on lateral flow and horizontal spreading of plume head material. The rate of accumulation of the erupted material allows for rough estimates of some plume parameters such as volume, time and rate of ascent. The two latter parameters are basically derived from simplified analytical estimations of the ascent rate or, assuming continuity, from lateral spreading rates. These estimates are subject to large uncertainties. For example, the constant Newtonian viscosity model by [35] provides estimates for the ascent rates on the order of 0.25 m/yr. Models based on temperature-dependent Newtonian viscosity by [36] provide ascent rates on the order of 1–2 m/yr. Finally, the non-Newtonian models with strain rate-dependent viscosity by [37] allow for several orders of magnitude higher ascent rates (hundreds and thousands m/yr). The same would apply to horizontal spreading rates, with the additional complication that the solution of the commonly used channel flow equations in the approximation of the lubrication theory de-

pend not only on the fluid rheology but also on the mechanical properties of the channel walls, i.e. on those of the lithosphere (e.g. [9,10]). The analytical and numerical estimates of plume dynamics appear to be quite approximate, in particular due to the strong dependence of the results on temperature and rheological assumptions, and also because the mechanical behaviour of the overlying lithosphere is usually neglected. Consequently, it is difficult to compare or to test various models on the basis of the previously predicted ascent rates. The observed surface topography and surface deformation (localised faulting or extension/compression zones) turn out to be one of the most

important constraints on the plume dynamics. A model that accounts for the free upper surface boundary condition and lithospheric rheology is thus highly needed.

### 1.5. Suggested model of plume–lithosphere interaction

We present a thermomechanical numerical model based on the fully explicit dynamic Lagrangian algorithm Parovoz [38] derived from the FLAC algorithm [39]. Parovoz explicitly takes into account the physical (non-linear elastic–brittle–ductile) properties of the mantle, crust and

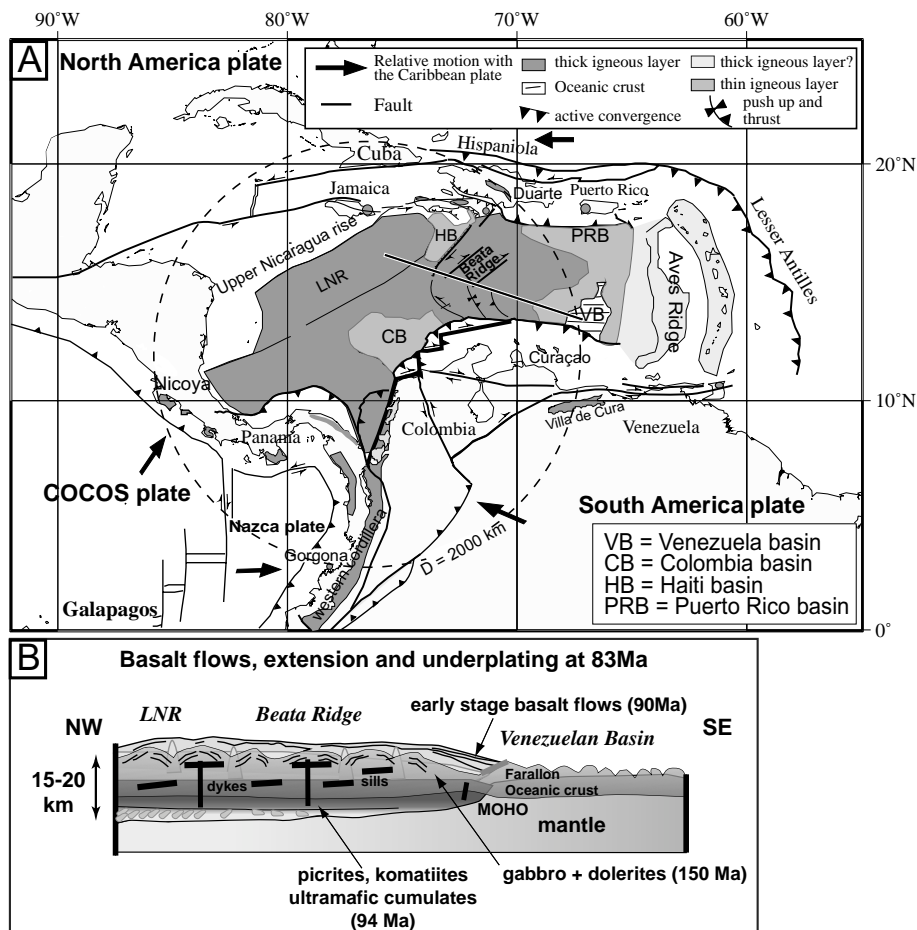


Fig. 1. (A) The Caribbean large igneous province is formed by the volcanic basement beneath the Caribbean Sea and several fragments accreted to the adjacent lands. (B) Interpretative crustal section at Santonian time (83 Ma) across the CLIP from the present Lower Nicaragua Rise (LNR), Beta ridge and Venezuelan basin. The ages of the different rocks come from a diving submersible survey [45,46] and ODP–DSDP results [40,41].

lithosphere. In particular, this algorithm: (1) uses an explicit ('true') free upper surface boundary condition; (2) uses explicit ('true') plasticity, elasticity and non-Newtonian power law viscosity, and (3) handles brittle and ductile strain localisations, which allows for simulation of formation of brittle faults and ductile shear zones. The algorithm allows us to make use of the data on temperature structure, velocity, composition, lithospheric strain and stress distributions.

## 2. The input data: The Caribbean LIP

Data on the thermomechanical behaviour of this magmatic plateau provide key input parameters for the numerical modelling, such as the size and depth of the initial plume, the initial temperature anomaly, and the thickness of the lithosphere and the crust.

The petrology and geochemistry of volcanic rocks reflect the depths and extent of mantle melting, both of which are controlled by the source temperature [3,29]. We can also extract more information on the formation of this LIP from the geophysical data. The input parameters chosen for the simulation were derived from data on the oceanic Caribbean LIP (CLIP).

The Caribbean plate (Fig. 1) is a magmatic province formed above the Galapagos hotspot during the Late Cretaceous [40,41]. Since then, it moved towards the east with respect to the American plates and started to collide with the North American plate during Campanian and Maastrichtian times (Fig. 1; [42]). The crust of CLIP, in the central part of the Caribbean plate (Beata ridge; Fig. 1) can be 20 km thick ([43] and references therein) and is composed of three main layers [44], from surface to bottom (Fig. 1): (1) a basaltic upper layer, (2) the initial oceanic crust (Farallon plate), (3) the underplated material made of gabbroic and ultramafic rocks (picrites, komatiites). Crustal thickness decreases to the east, in the Puerto Rico basin, to 10–15 km and becomes less than 5 km in the Venezuela basin underlain by the old oceanic crust. The edge of the CLIP in the Venezuela basin is formed by a wedge of flood basalts observed on the seismic

profiles by a seaward-dipping reflector prism (Fig. 1B; [45]).

The Galapagos hotspot magmatic activity on the Farallon plate has been recorded between 90 and 75 Ma with two major magmatic events; the first one at 90–88 Ma and the second one at 75 Ma. Both events correspond to emplacement of underplated and basaltic rocks ([46] and references therein). According to the geochemical, structural and geophysical studies of the CLIP ([44,45] and references therein) and particularly of the outcrops in Hispaniola and the Curaçao islands, we can assume that the proto-Caribbean crust has an initial thickness of about 6 km and an age of 150 Ma corresponding with the Farallon oceanic crust. The picrites from Curaçao indicate a moderate formation depth beneath a relatively old and thick lithosphere (60 km) [47]. Furthermore, the width of the CLIP is constrained by the location of the igneous rocks identified as related to the Galapagos hotspot activity. A 2000 km diameter circle drawn on the map of the CLIP (Fig. 1) is tangent to the komatiites of Gorgona, the picrites of the Nicoya peninsula, Duarte and Curaçao, and to the Venezuelan basin. It does not include the whole igneous province, i.e. some parts are missing in the southeast particularly [46].

Finally, for the initial model, the age and the thickness of the oceanic lithosphere are settled on 60 Ma and on 90–100 km, respectively [23,47].

## 3. Numerical model

### 3.1. Algorithm

#### 3.1.1. Equations solved

Parovoz is a '2.5D' numerical scheme, in which the coordinate frame is Cartesian 2D, but all stress/strain relations are computed in full 3D formulation. Parovoz is a large-strain, fully explicit, time-marching Lagrangian algorithm that locally solves full Newtonian equations of motion in a continuum mechanics approximation:

$$\left\langle \rho \frac{\partial}{\partial t} \left( \frac{\partial \mathbf{u}}{\partial t} \right) \right\rangle - \text{div} \boldsymbol{\sigma} - \rho \mathbf{g} = 0 \quad (2)$$

coupled with constitutive equations of the follow-

ing kind:

$$\frac{D\sigma}{Dt} = F\left(\sigma, \mathbf{u}, \nabla \frac{\partial \mathbf{u}}{\partial t}, \dots, T, \dots\right) \quad (3)$$

and with those of heat transfer:

$$\rho C_p \partial T / \partial t + \mathbf{u} \nabla T - \text{div}(\mathbf{k} \nabla T) - H_r = 0 \quad (4)$$

Here  $\mathbf{u}$ ,  $\sigma$ ,  $\mathbf{g}$ ,  $\mathbf{k}$  are the respective vector–matrix terms for the displacement, stress, acceleration due to body forces and thermal conductivity. The angular brackets in Eq. 2 mean conditional use of the respective term (i.e. in quasi-static mode inertial terms are surprising using inertial mass scaling [39]). The terms  $t$ ,  $\rho$ ,  $C_p$ ,  $T$  and  $H_r$  designate time, density, specific heat, temperature and internal heat production, respectively. The terms  $\partial/\partial t$  (in Eq. 2),  $D\sigma/Dt$ ,  $F$  (in Eq. 3) denote a time derivative, an objective time derivative and a functional, respectively. In the Lagrangian method, the incremental displacements are added to the grid coordinates allowing the mesh to move and deform with the material. Consequently, the deformation is always small with respect to the local coordinate frame, which moves together with the material, allowing one to use a small-strain formulation of the governing equations for solution of large-strain problems (in each time step the solution is obtained in local coordinates, which are then updated in the large-strain mode). In each time step the algorithm checks and adjusts the internal time step to assure a stable solution. Due to an explicit approach, there are no convergence issues for non-linear rheologies, which is a typical problem of implicit methods. The FLAC method can thus handle physically extremely unstable processes and wildly non-linear rheologies.

### 3.1.2. Explicit plastic–elastic–viscous rheology

Instead of pseudoplasticity and pseudoelasticity (e.g. [19,21]), we use the explicit form of elastic–ductile–plastic rheologies provided by rock mechanics data [48]. The total strain increment in each numeric element is thus defined by the sum of elastic, viscous and brittle strain increments.

**3.1.2.1. Plastic (brittle) behaviour.** This behaviour is described by Byerlee's law [24,49]:

$$\begin{aligned} \tau &\approx 0.85\sigma_n && \text{if } \sigma_n < 200 \text{ MPa;} \\ \tau &\approx 0.5 \text{ MPa} + 0.6\sigma_n && \text{if } \sigma_n > 200 \text{ MPa} \end{aligned} \quad (5)$$

where  $\tau$  is shear stress and  $\sigma_n$  is normal stress. Byerlee's law corresponds to a pressure-dependent Mohr–Coulomb material with friction angle  $\phi$  and cohesion  $|C_0|$  (e.g. [26]):

$$|\tau| = C_0 - \sigma_n \tan \phi \quad (6)$$

where  $\sigma_n = P + \sigma_{II}^{\text{dev}} \sin \phi$ ,  $P$  is the effective pressure,  $\sigma_{II}^{\text{dev}}$  is the second invariant of deviatoric stress, or effective shear stress. The condition (function) of rupture is:  $f = \sigma_{II}^{\text{dev}} + P \sin \phi - C_0 \cos \phi = 0$  and  $\partial f / \partial t = 0$ . Parameters  $\phi = 30\text{--}33^\circ$  and  $|C_0| = 5\text{--}20$  MPa represent typical rocks.

**3.1.2.2. Elastic behaviour.** The elastic part is defined using Lamé's constants  $\lambda = \mu = 32$  GPa equivalent to Young's modulus,  $E$ , of 80 GPa and Poissons's ratio,  $\nu$ , of 0.25 [26]:

$$\sigma_{ik} = (\lambda + 2\mu) \varepsilon_{II} \delta_{ik} + 2\mu (\varepsilon_{ik} - 3^{-1} \varepsilon_{II} \delta_{ik}) \quad (7)$$

**3.1.2.3. Viscous (ductile) behaviour.** Creeping flow in the mantle [49,50] strongly differs from Newtonian flow since the effective viscosity can vary within 10 orders of magnitude as a function of differential stress, even at adiabatic temperature conditions:

$$\dot{\varepsilon} = A (\sigma_1 - \sigma_3)^n \exp\left(-\frac{Q + PV}{RT}\right) \quad (8)$$

where the parameters  $A$ ,  $n$ ,  $Q$  are material constants (see Table 2),  $\sigma_1$  and  $\sigma_3$  are the principal stresses,  $\dot{\varepsilon}$  is the strain rate,  $T$  is the absolute temperature, and  $R$  is the universal gas constant. For olivine parameters (Table 2), the predicted effective viscosity at the base of the lithosphere is  $10^{19}\text{--}5 \times 10^{19}$  Pa s, which is close to postglacial rebound data [23]. Within the lithosphere, the effective lithospheric viscosity grows from  $10^{19}$  at the base to  $10^{25}\text{--}10^{27}$  Pa s at the brittle–ductile transition. The deep mantle viscosity is  $10^{20}\text{--}10^{21}$  Pa s (e.g. [8]). However, Weinberg and Podladchikov [37] have shown that the effective viscosity in the vicinity of a diapir is primarily influenced by the local strain rate field and partly by heat exchanges with surrounding rock.

To handle physical instabilities, it is sufficient to assign lower viscosity cutoff at a two orders of

magnitude lower value ( $10^{18}$  Pa s) than its average bulk viscosity. The upper viscosity cutoff was kept at  $10^{27}$  Pa s. This allows us to handle the whole range of lithospheric stresses (10 MPa–1 GPa) and tectonic strain rates ( $10^{-18}$ – $10^{-12}$  s $^{-1}$ ; e.g. [23]).

### 3.2. Problem setup, physical, mechanical and spatial properties

The lithosphere–plume interactions are largely confined within the first 300 km from the surface [8]. Following previous studies [8], we limited the vertical size of the model to 400 km. At 300–400 km depth, the temperature, density, pressure, stress and velocity are poorly constrained allowing for 20–40% uncertainties [3,4,51–53]. We thus had to choose a reference parameter model (Table 1). Based on this model, we varied sensitive parameters such as density, temperature and viscosity to evaluate their effects on the lithosphere–plume interaction as well as for comparison with previous studies.

Two different box sizes for the numerical sim-

ulations were used (Fig. 2). The first reference model refers to the Caribbean igneous province and comprises a 2000 km  $\times$  400 km rectangular box with a spherical initial thermal anomaly of 300 km in diameter (Fig. 2). To gain computing time, we also used a smaller (1000 km  $\times$  400 km) box with an initial plume diameter of 165 km (Fig. 2). All models include three horizontal brittle–elastic–ductile layers (Tables 1 and 2; [50]): (1) a 6 km thick crust with a density of 2900 kg/m $^3$ ; (2) a 100 km thick lithosphere with a density of 3300 kg/m $^3$ ; and below it, (3) the asthenosphere/deeper mantle with a density growing from 3300 kg/m $^3$  at normal conditions to 3540 kg/m $^3$  at the bottom of the box [23]. A non-uniform grid of 201  $\times$  94 elements provides a vertical resolution of 2.5 km/element in the crust, of 3 km/element in the lithosphere and of 5 km/element in asthenospheric mantle, and a horizontal resolution of 10 km/element (reference model) or 5 km/element (high-resolution test model). The lithospheric layer thus counts 34 elements in the vertical direction, which implies a 10–15 times higher resolution than in common models (e.g. [8]).

Table 1  
Notation and values used in simulations

Parameter	Value and unit	Definition
$h_c$	6 km	Moho depth
$y, h_l$	100 km	depth of lithosphere
$\rho_c$	2900 kg/m $^3$	crustal density
$\rho_m$	3300 kg/m $^3$	mantle density
$g$	9.8 m/s $^2$	acceleration of gravity
$k_c$	2 W m $^{-1}$ K $^{-1}$	thermal conductivity of the crust
$k_m$	3.3 W m $^{-1}$ K $^{-1}$	thermal conductivity of the mantle
$C_p$	10 $^3$ J kg $^{-1}$ °C $^{-1}$	specific heat
$\lambda$	3 $\times$ 10 $^{10}$ Pa	first Lamé parameter
$\mu$	3 $\times$ 10 $^{10}$ Pa	second Lamé parameter (shear modulus)
$\alpha$	3 $\times$ 10 $^{-5}$ °C $^{-1}$	thermal expansion
$\eta$	10 $^{19}$ –10 $^{25}$ Pa s	viscosity
$\eta_r$	10 $^{20}$ and 10 $^{21}$ Pa s	asthenospheric viscosity
Reference model		
$l_r$	2000 km	box length
$\phi_{ref}$	300 km	plume diameter
$\Delta T_{ref}$	300 °C	temperature contrast plume–mantle
$\Delta \rho_{ref}$	30 kg/m $^3$	density contrast plume–mantle
Test model		
$l_{test}$	1000 km	box length
$\phi_{test}$	160 km	plume diameter
$\Delta T_{test}$	100, 300, 500, 1000 °C	temperature contrast plume–mantle
$\Delta \rho_{test}$	10, 30, 50, 100 kg/m $^3$	density contrast plume–mantle

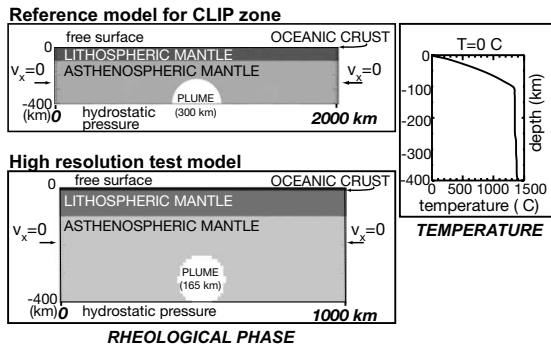


Fig. 2. Model setup. Large-scale reference model (top) and higher-resolution test model (bottom). Shown are the phase fields on the non-uniform  $201 \times 94$  grid. Initial temperature profile (right).

The elastic and brittle properties are the same for all layers. The ductile rheological terms are defined using basalt and olivine creep flow laws for the crust and mantle, respectively (Table 2; [48,49]).

Following [8] we do not consider the initial stages of diapir formation. The initial plume presents a spherical thermorheological anomaly with a diameter of 300 km (reference calculation) or 165 km (test simulations) located at a depth of 400 km [8]. The assumption of initially spherical geometry is justified because in an infinite medium, a finite body rising in a laminar regime keeps a spherical shape. In middle mantle conditions, diapir ascent occurs at small Reynolds number and thus in the laminar regime. This assumption also allows for comparison with previous studies [8,37,54]. In the reference calculations, the initial temperature anomaly  $\Delta T$  and the equivalent density contrast between the plume and the mantle were, respectively,  $300^\circ\text{C}$  and  $30 \text{ kg/m}^3$  [8,51]. In test simulations, we varied these parameters in a wide range of values from 100 to  $1000^\circ\text{C}$ , and from 10 to  $100 \text{ kg/m}^3$ , respectively, following [55].

The initial thermal structure of the mantle (Fig.

2) is defined using the commonly inferred thermal profile with age-dependent conductive geotherm in the lithosphere and near-adiabatic temperature gradient in the mantle. The bottom of the lithosphere is placed at a depth of  $1330^\circ\text{C}$ . Below this depth, the temperature slowly increases from  $1330$  to  $1400^\circ\text{C}$  at 400 km depth (e.g. [8]).

For oceanic lithosphere, the initial geotherm is given by the analytical solution for a cooling half-space [23]:

$$T = T_b \text{erf}(\gamma(4\chi t_1)^{-1/2}) \quad (9)$$

where  $\gamma$  is the lithosphere thickness,  $T_b = 1330^\circ\text{C}$ ,  $\chi$  is the thermal diffusivity ( $\chi = 10^{-6} \text{ m}^2/\text{s}$ ),  $t_1$  is the age of the lithosphere (60 Ma according to CLIP data).

The depth interval of brittle–ductile transition is outlined by isotherms  $T = 400^\circ\text{C}$  and  $750^\circ\text{C}$  [56]. In our case, Eq. 9 predicts that the thickness of the upper brittle (seismogenic) layer in the lithosphere is 30–50 km.

Simple boundary conditions are assigned on the four sides of the box (Fig. 2). On the left and right sides, horizontal velocity is  $v_{xx} = 0$ . At the bottom, hydrostatic pressure is applied with a reference density  $\rho = 3540 \text{ kg/m}^3$  corresponding to 400 km depth. A free surface is the upper boundary condition.

## 4. Results and experiments

### 4.1. Preliminary theoretical considerations

The mechanics of plumes and diapirs was investigated in a number of studies (e.g. [37] and references therein). Most theoretical models consider a spherical diapir whose ascent velocity is given by solution of the Stokes problem for different assumptions on the viscous rheology and heat balance with the background. Since the solution is obtained for an infinite space, the estimated as-

Table 2  
Parameters for dislocation creep

Mineral–rock	$A$ ( $\text{Pa}^{-n} \text{ s}^{-1}$ )	$Q$ (kJ/mol)	$n$	Reference
Basalt–diabase (dry)	$6.31 \times 10^{-20}$	276	3.05	Carter and Tsenn [64]
Olivine–dunite (dry) dislocation climb at $(\sigma_1 - \sigma_3) \leq 200 \text{ MPa}$	$7 \times 10^{-14}$	520	3	Kirby and Kronenberg [50]

cent rates are applicable only to large depths (plume initiation).

For simple Newtonian viscosity and an isothermal spherical plume, Stokes' law provides an estimate for the ascent velocity  $v_s$  determined from the ratio of the positive buoyancy force  $f_a$  to the viscous drag force  $f_v$ . The ratio  $f_a/f_v$  should be  $\geq 1$  to initiate ascent,  $f_a = \Delta\rho g(4/3\pi r^3)$  and  $f_v = 6\pi r\eta v_s$ , which yields Stokes' ascent velocity:

$$v_s = (2/9)\Delta\rho g r^2 \eta^{-1} \quad (10)$$

where  $\eta$  is the mean viscosity of the surrounding material,  $\Delta\rho$  is the density contrast (from 10 to 100 kg/m<sup>3</sup>),  $g$  is the acceleration due to gravity,  $r$  is the plume radius. Assuming the characteristic heat diffusion time  $t_d = r\chi^{-1}$  and the ascent time  $t_a = (d-h)/v_s$ , where  $\chi$  is thermal diffusivity,  $d$  is the initial plume depth and  $h$  its final depth below the lithosphere, one should require  $t_d \gg t_a$  for successful ascent of a hot plume. Eq. 10 predicts low ascent rates of 0.2–0.5 m/yr. Temperature-dependent Newtonian viscosity provides higher but still not important ascent rates of 1–2 m/yr. Yet the effective viscosity of real rocks is not only temperature- but also largely strain rate-dependent. According to the approximation derived in [37] for non-Newtonian embeddings, the effective viscosity  $\eta_{\text{eff}}$  and the ascent rate  $v_y$  can be estimated assuming characteristic buoyancy-driven stress  $\sigma = \Delta\rho g r$  (i.e.  $f_a = \int_v \sigma dV$ ) and the flow law (Eq. 8) with neglected  $PV$  term:

$$\partial\varepsilon/\partial t = \sigma^n A \exp(-Q/RT) \quad (11)$$

$$\eta_{\text{eff}} = (6^{n-1} \exp(Q/RT)) / (3^{-(n-1)} A (\Delta\rho g r)^{n-1}) \quad (12)$$

$$v_y = \Delta\rho g r^2 / 3\eta_{\text{eff}} = 3^{-(n-1)} r A (\Delta\rho g r)^n / (3 \cdot 6^{n-1} \exp(Q/RT)) \quad (13)$$

We assume that  $\Delta\rho = \Delta\rho_c + \alpha\rho_0\Delta T$ , where  $\Delta\rho_c$  and  $\Delta T$  are, respectively, the chemical density and temperature contrast between the plume and its embeddings,  $\rho_0$  is the density of embeddings at temperature  $T$ ,  $\alpha$  is the coefficient of thermal expansion ( $3 \times 10^{-5} \text{C}^{-1}$ ). Assuming plausible (see previous section) parameters, we obtain ascent rates as high as 10–5000 m/yr. The temperature and softening of the wall-rock is conditioned by

heat transfer from the plume, yet neglected in Eq. 13 derived for fast ascent at great depth occurring with low heat loss. In the final ascent stage, the heat loss is important because the ascent rate drops dramatically due to (1) the free upper surface, (2) increasing resistance of colder surrounding rocks, and (3) decreasing density contrast.

The Reynolds number for a plume,  $Re_p$ , which characterises its tendency to turbulent regime and deviation from the initial spherical shape, can be estimated as:

$$Re_p \approx 2r(\rho_0(1 + \alpha\Delta T) + \Delta\rho_c) v_y / \eta_{\text{eff}} = 2(1 + \rho_0(\Delta\rho_c + \alpha\rho_0\Delta T)^{-1}) (\Delta\rho_c + \alpha\rho_0\Delta T)^2 g r^3 / 3\eta_{\text{eff}}^2 \quad (14)$$

In our case  $Re_p$  is less than  $10^{-18}$ . The ascent thus starts in the laminar regime, which justifies the assumption of an initially spherical plume. The important dependence of  $\eta_{\text{eff}}$  on depth and temperature does not allow us to derive a unique Rayleigh number for the whole system. Of course one can introduce a combination of surface, local and bottom Rayleigh numbers (e.g. [21]). Yet for our experiments, it is more convenient to use a single parameter. We thus introduce an effective Rayleigh number for the plume. Let us assume an ascent interval  $d-h$  and a maximal driving density contrast  $\Delta\rho_{\text{max}}$ , where  $d$  is the depth to the bottom of the mantle,  $h$  is the depth to the bottom of the lithosphere,  $\Delta\rho_{\text{max}} = (\rho_p \alpha \Delta T_{\text{max}} + \Delta\rho_c)$  with  $\rho_p$  being the density of plume material at embedding temperature at depth  $d$ , and  $\Delta T_{\text{max}}$  the difference between temperatures of plume material at depths  $d$  and  $h$ . Assuming some representative mean temperature  $T^*$ , a simplified approximation for plume Rayleigh number,  $Ra_p$ , reads:

$$Ra_p \approx g \Delta\rho_{\text{max}} (d-h)^3 / \chi \eta_{\text{eff}}(r, T^*, \Delta\rho) = 3^{-(n-1)} A g^n \Delta\rho_{\text{max}} (r(\Delta\rho_c + \alpha\rho_0\Delta T))^{n-1} (d-h)^3 / (\chi \cdot 6^{n-1} \exp(Q/RT^*)) \quad (15)$$

Instead of  $Ra_p$ , a local depth/temperature-dependent Rayleigh number  $Ra_b$  can also be introduced by replacing  $d-h$  with a diffusion length scale  $\delta = (\pi\chi t_{\text{cr}})$ ;  $\Delta\rho_{\text{max}}$  with  $\Delta\rho$ ;  $\Delta T_{\text{max}}$  with  $\Delta T$ ;

and  $T^*$  with  $T$ , where  $t_{\text{cr}}$  can be found from equating  $Ra_b$  to critical value  $Ra_{\text{cr}}$  for onset of Rayleigh–Taylor instability ( $Ra_{\text{cr}} \approx 3 \times 10^3$ ) or by choosing some other characteristic length scale  $\delta_1$  and assuming  $t_{\text{cr}} = \delta_1^2/\chi$ .

For a Newtonian fluid,  $Ra_p$  is a linear function of density contrast and does not depend on the plume size. In case of a non-Newtonian fluid with  $n=3$  (Table 2),  $Ra_p$  scales as a third power of the density/temperature contrast and as a second power of the plume size  $2r$ . Ascent through a non-Newtonian fluid is thus extremely sensitive to effective body forces. A small variation in buoyancy force results in strong variation in plume behaviour. For the same body force, the ascent rate may be orders of magnitude faster than for a Newtonian fluid.

The lithosphere, at which base the flattening of the plume head begins, is not entirely viscous, but brittle–elastic–ductile. Theoretically, a hot plume can ascend through the lithosphere in the ductile aureole produced by its own heat. Yet the plume velocity will be slow as limited by the characteristic diffusion time  $t_d$ . However, heat diffusion rate and thermal buoyancy cannot solely control the diapiric ascent rate near the upper brittle–ductile boundary layer [57]. In this layer, flexural and basal shear stress created by the ascending plume result in its extension and necking, i.e. localised thinning above the plume. Models of active rifting [13] suggest that the plume head can be advected in the space created by lithospheric necking. Necking can be a rapid process, and the resulting total ascent rate can be much higher than that of heat diffusion. The estimation of the near-lithosphere ascent rate is thus not a trivial matter and requires a numerical approach.

## 4.2. Plume–lithosphere interaction

### 4.2.1. Preliminary tests

We first tested the numerical model using the analytical solution of vertical ascent (Eq. 15) in infinite space. This solution does not account for heat diffusion, so the driving force is constant. For this reason a constant density contrast from 10 to 100 kg/m<sup>3</sup> was used for this set of tests, and the temperature varied from 900 to 2000°C. The

computed ascent velocities in the middle of the computing area closely matched analytical predictions, with 2–5% differences related to finite area, viscosity cutoff and other unavoidable inherent differences between the analytical and numerical model conditions.

Another series of test experiments was aimed at reproducing the vertical uplift for particular conditions (assumption of local isostasy, fixed upper surface, etc.) of commonly referred numerical experiments by [8]. The predicted purely local isostatic uplift matches predictions of [8] within less than 10% discrepancy. We consider this as a very good fit knowing that the numerical code used in [8] has some non-documented procedures for handling effective viscosity variations that cannot be reproduced exactly (A. Tagi-Zade, personal communication, 2002).

### 4.2.2. Plume head flattening

In the experiments shown in Figs. 3 and 4, the temperature, density and viscosity anomalies (Table 1) cause rapid ascent of the plume in less than 0.5–2 Ma, so that the plume preserves most of its thermal energy when it arrives at the bottom of the lithosphere. From this moment, thermal and mechanical evolution of the lithosphere starts to be progressively controlled by its interaction with the plume head.

Plume head flattening begins as soon as its upper extremity reaches the bottom of the lithosphere. Peculiar features of this process can be observed in the strain rate, velocity, temperature, shear stress and phase fields (Fig. 3). The velocity field shows two distinct convective cells (velocity field) and lobes (chemical phase field) situated on either side of the plume head and present only in the asthenospheric mantle. The strain rate field shows two areas of strain localisation at the bottom of the lithosphere above the plume head (Fig. 3B). The cells erode some cool material from the base of the lithosphere and drag it down in the asthenospheric mantle on the edge of the plume head (see phase, velocity and temperature fields in Fig. 3). This erosion primarily occurs due to strain rate weakening and not due to thermal softening, which needs more time. The shear stress field predicts stress localisations on the order of

$\pm 50$ – $110$  MPa within the first 50 km of the lithosphere, which remains effectively elasto-plastic and non-viscous (Fig. 3C). High shear stresses are also localised above the rising plume and both edges of the plume head (Fig. 3C). The plume head, which had an initial diameter of 300 km, becomes 1000 km wide under the lithosphere (Fig. 3A). Its horizontal spreading rate  $v_x$  is maximal between 0.5 and 1 Ma, when it reaches 0.2–0.3 m/yr, and then decreases to 0.1–0.2 m/yr between 1 and 1.6 Ma (Fig. 3F). These spreading

rates are compatible with the data on CLIP (see below).

In Fig. 4, we have summarised different test simulations, in which we varied the minimal effective Rayleigh number  $Ra_p$  (equation 15) for the plume ascent from  $10^4$  to  $10^6$ . Note that  $Ra_p$  is relatively small because it is calculated for a vertical box size of 400 km. A larger vertical box size (e.g. 660 km) would impose  $Ra_p$  values on the order of  $10^5$ – $10^7$ .  $Ra_p$  integrates the effect of variation of three parameters: viscosity, temperature

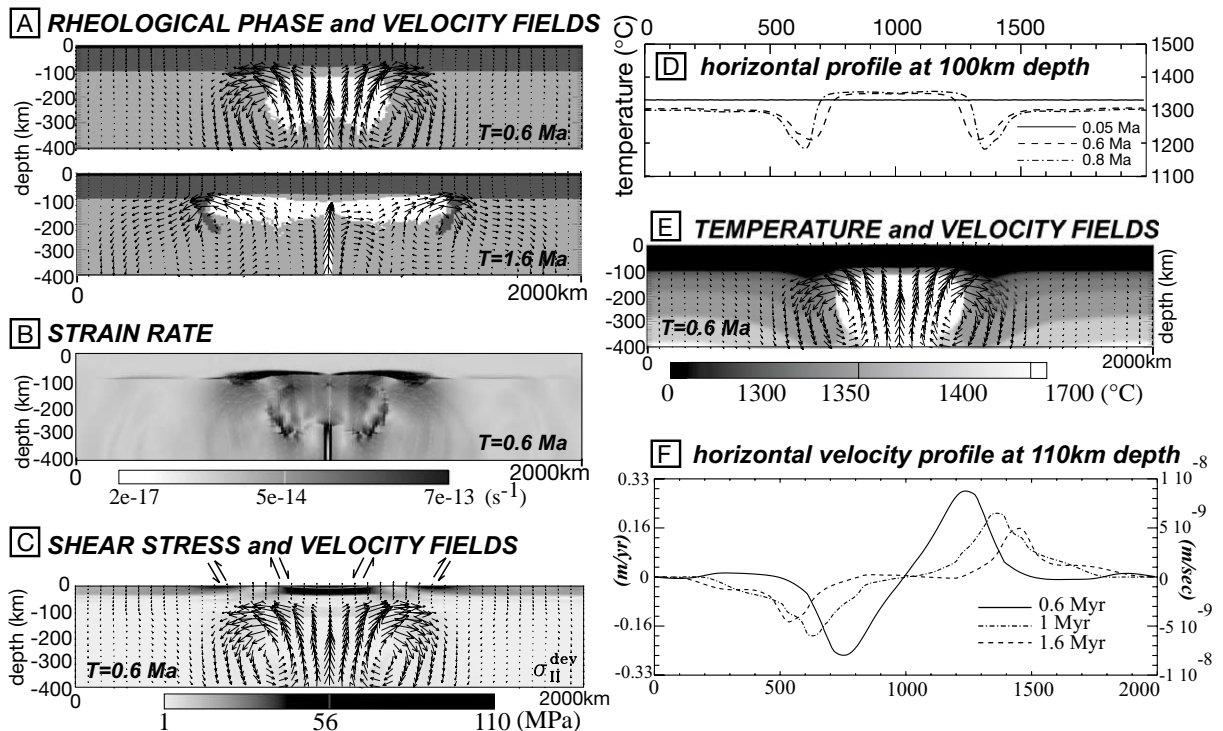


Fig. 3. Experiments on plume–lithosphere interaction (reference model). (A) Rheological phase and velocity fields. The plume head reaches the bottom of the lithosphere and begins flattening. Maximal vertical velocity at  $t=0.1$  Ma is 5 m/yr. At the moment of emplacement (0.5–0.6 Ma) it drops to 0.3 m/yr. At  $t=1.6$  Ma (maximum velocity is 0.2 m/yr), the phase field shows a plume head flattening on a 1000 km scale bounded by two areas of downward lithospheric instabilities. Horizontal spreading rates reach 0.5–1 m/yr at  $t=0.6$  Ma. The erosion of the lithosphere spreads over a 1000 km wide region, the thickness of the lithosphere decreases from 100 to 70–80 km. (B) Strain rate field at 0.6 Ma. The highest strain rate areas are located in two zones adjacent to the axial zone. (C) Effective shear stress (second stress invariant) at 0.6 Ma. Note that large values develop near the surface, which lead to faulting. (D) Temperature cross-section at the bottom of the initial isothermal lithosphere for various simulation times. At 0.6 and 0.8 Ma the lithosphere above the plume head (between 700 and 1300 km) gets thinner with the strong uprise of the  $1300^{\circ}C$  isotherm. At the edges of the plume head there are two zones of cooling due to downward movement of the lithospheric material, about 200 km wide. In bordering regions between  $x=0$ –500 km and  $x=1500$ –2000 km a distinct decrease of the lithospheric geotherm is observed. (E) Temperature rise on the edge of the plume head at 0.6 Ma. No vertical exaggeration.

and density. Depending on these parameters, the plume head reaches the base of the lithosphere at remarkably different rates (Fig. 4). Similarly, depending on the parameters used, the plume head flattens at highly different horizontal velocities (Fig. 4) and takes different geometries. Of course a single parameter is not sufficient to describe the behaviour of a strongly non-Newtonian fluid. For example, for the same values of  $Ra_p$ , the ascent and spreading velocities of the plume head are much higher for an average asthenospheric viscosity of  $10^{20}$  Pa s than for the cases where it is limited to  $10^{21}$  Pa s (Fig. 4). The increase in the amplitude of initial temperature and density anomaly leads to specific triangular plume head geometries resulting from strong strain localisation above its head (Fig. 4).

#### 4.2.3. Thermomechanical erosion of the lithosphere

Previous studies [58,59] suggest that the plume head can erode the base of the lithospheric mantle. Davies [59] has suggested that the velocity and the rate of thinning should strongly depend on the lateral scale of the upwelling defined by the length of the plume head flattening, and that rapid thinning is favoured by the small horizontal scale of the upwelling and by low mantle viscosities. Yet [58] and [60] find the erosion to be rather slow unless the viscosity under the lithosphere is extremely low. Van Keken [52] has also found that a non-Newtonian rheology permits a much more rapid ascent and a more elevated temperature of the plume, which, in turn, causes a more efficient production of flood basalt than in the case of a Newtonian rheology. At this point, our experi-

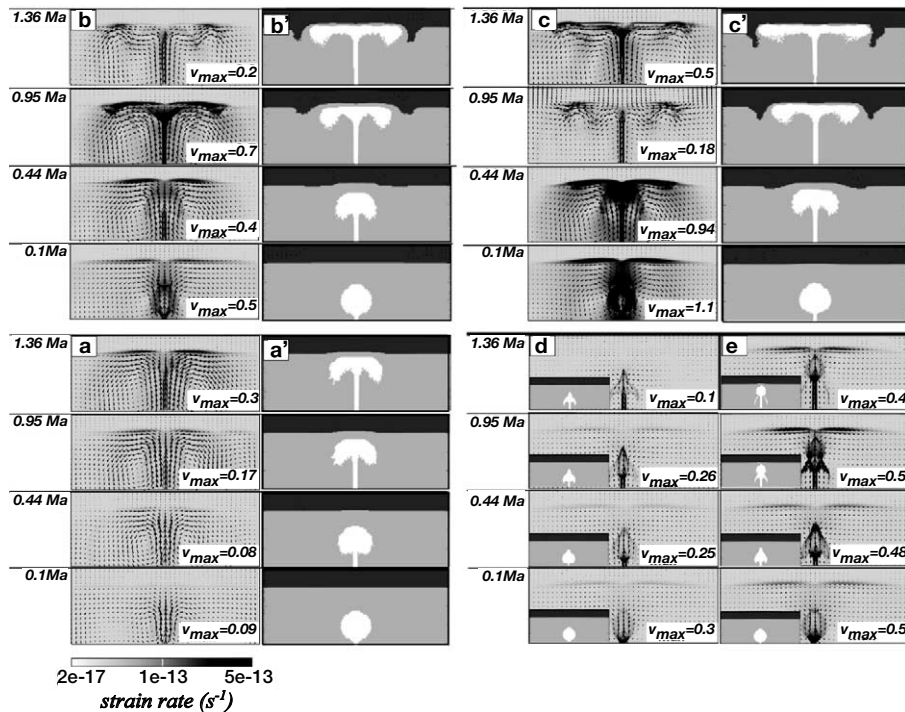


Fig. 4. Test models. Representative cases demonstrating variation with time of the plume ascent velocity field (arrows), of the strain rate (a–e) and the rheological phase field (a'–c' and inserts d and e), for different values of effective plume Rayleigh number (Eq. 15) resulting from variation of the temperature contrast, density and minimal viscosity. No vertical exaggeration,  $1000 \times 400$  km box,  $v_{max}$ : maximum velocity (m/yr). Strain rate field correlates with the velocity field. (a–a')  $Ra_p = 1.56 \times 10^5$  ( $\Delta T = 100^\circ\text{C}$ ,  $\Delta\rho = 10 \text{ kg/m}^3$ ,  $\eta = 10^{20}$  Pa s). (b–b')  $Ra_p = 2.7 \times 10^5$  ( $\Delta T = 300^\circ\text{C}$ ,  $\Delta\rho = 30 \text{ kg/m}^3$ ,  $\eta = 10^{20}$  Pa s). (c–c')  $Ra_p = 3.64 \times 10^5$  ( $\Delta T = 500^\circ\text{C}$ ,  $\Delta\rho = 50 \text{ kg/m}^3$ ,  $\eta = 10^{20}$  Pa s). (d) Lower Rayleigh number test:  $Ra_p = 3.64 \times 10^4$  ( $\Delta T = 500^\circ\text{C}$ ,  $\Delta\rho = 50 \text{ kg/m}^3$ ,  $\eta = 10^{21}$  Pa s). (e) Lower Rayleigh number test:  $Ra_p = 6.24 \times 10^4$  ( $\Delta T = 1000^\circ\text{C}$ ,  $\Delta\rho = 100 \text{ kg/m}^3$ ,  $\eta = 10^{21}$  Pa s).  $\Delta\rho$  is the total density contrast between the plume and the surrounding material in the starting position at the bottom.

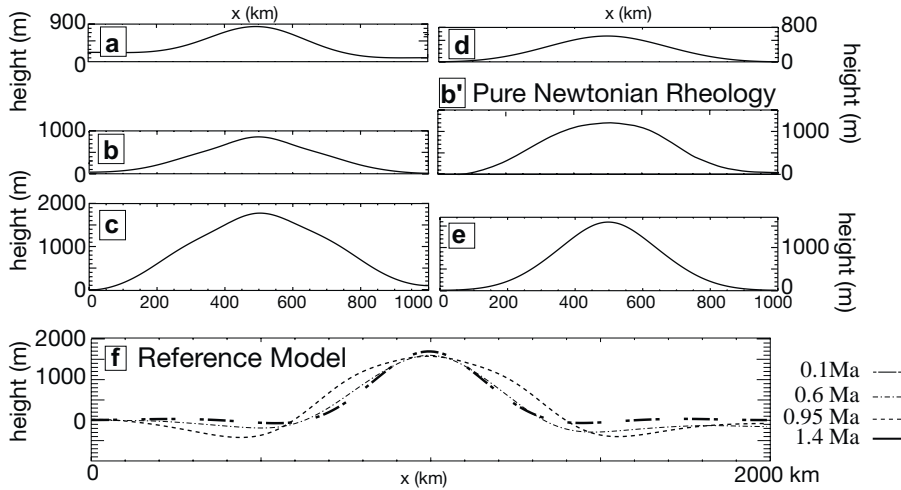


Fig. 5. Surface topography between 0.1 and 1.4 Ma. (a–e) Test model horizontal scale 1000 km corresponding to the case of Fig. 4 at 1.4 Ma. (a) Lower Rayleigh number test:  $Ra_p = 1.56 \times 10^5$  ( $\Delta T = 100^\circ\text{C}$ ,  $\Delta\rho = 10 \text{ kg/m}^3$ ,  $\eta = 10^{20} \text{ Pa s}$ ). (b)  $Ra_p = 2.7 \times 10^5$  ( $\Delta T = 300^\circ\text{C}$ ,  $\Delta\rho = 30 \text{ kg/m}^3$ ,  $\eta = 10^{20} \text{ Pa s}$ ). (c)  $Ra_p = 3.64 \times 10^5$  ( $\Delta T = 500^\circ\text{C}$ ,  $\Delta\rho = 50 \text{ kg/m}^3$ ,  $\eta = 10^{20} \text{ Pa s}$ ). (b') Benchmark test assuming local isostasy with pure Newtonian rheology for the crust and the lithosphere ( $\Delta T = 300^\circ\text{C}$ ,  $\Delta\rho = 30 \text{ kg/m}^3$ ,  $\eta = 10^{20} \text{ Pa s}$ ). (d) Lower Rayleigh number test  $Ra_p = 3.64 \times 10^4$  ( $\Delta T = 500^\circ\text{C}$ ,  $\Delta\rho = 50 \text{ kg/m}^3$ ,  $\eta = 10^{21} \text{ Pa s}$ ). (e) Lower Rayleigh number test:  $Ra_p = 6.24 \times 10^4$  ( $\Delta T = 1000^\circ\text{C}$ ,  $\Delta\rho = 100 \text{ kg/m}^3$ ,  $\eta = 10^{21} \text{ Pa s}$ ). (f) Reference model:  $Ra_p = 2.66 \times 10^5$  ( $\Delta T = 300^\circ\text{C}$ ,  $\Delta\rho = 30 \text{ kg/m}^3$ ,  $\eta = 10^{20} \text{ Pa s}$ , horizontal scale 2000 km). For the reference case (f), the major long-wavelength dynamic surface uplift (1600 m) is recorded at 0.95 Ma. (a–e) The uplift decreases with the temperature, the density and the asthenospheric viscosity  $\eta_r$ .

ments (Fig. 3) support the previous studies. Yet, in strong contrast with them, our experiments suggest that the lithosphere is preferentially eroded in the centre only at the earliest stages, when the plume is not significantly flattened (Fig. 3). As the plume head flattens, the lithosphere is much more eroded in two large areas adjacent to the centre (Figs. 3 and 4), where the strain rates are highest. This favours formation of alternating zones of lithospheric extension and compression. The deformation increases under the lithosphere while these two areas reach higher strain rate values. In our reference and test models (Figs. 3 and 4), the plume–lithosphere interaction develops at very initial stages of plume ascent and starts from rapid thinning (phase fields in Figs. 3 and 4) and erosion (temperature and strain rate fields in Figs. 3 and 4) of the lithosphere, so that the lithosphere ‘feels’ the plume when it is still midway to the surface.

Simulations comparing the effect of different asthenospheric viscosities show that the plume velocity and the strain rate field are strongly dependent on the viscosity contrast (i.e. viscosity gra-

dient) at the transition between the lithosphere and underlying surrounding mantle (Fig. 4a–e). When the asthenospheric mantle viscosity is reduced by one order of magnitude (from  $10^{21}$  to  $10^{20}$  Pa s), the basal lithospheric erosion becomes stronger (Fig. 4c–c’) just as the lithospheric thinning also becomes more important and considerably faster (note the shorter time scale in Fig. 4c–c’). It thus appears that the strain rate is very dependent on the viscosity profile through the lithosphere–asthenosphere transition as well as on the plume–asthenosphere viscosity contrast. The vertical thinning rate appears to be only weakly dependent on the lateral scale of the upwelling, contrary to the geometry and evolution of the area of horizontal thinning, which is dependent on the length of the plume head flattening.

#### 4.2.4. Surface uplift

Surface topography variations obtained using a free surface boundary condition allow for more consistent examination of the impact of the plume–lithosphere interaction on the surface de-

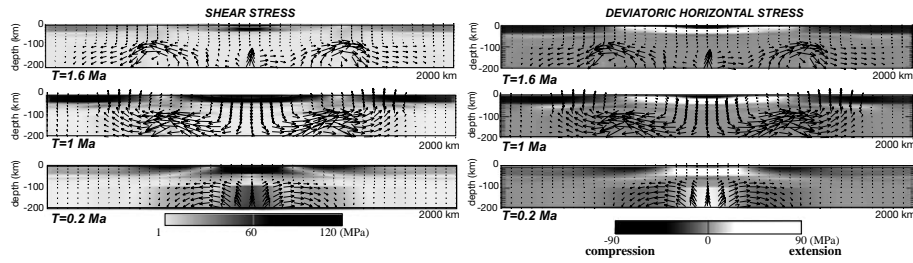


Fig. 6. Shear stress and deviatoric horizontal stress with velocity field between 0.2 and 1.6 Ma. The horizontal extensional area localised within the elasto-plastic part of the lithosphere widened from 0.2 to 1.6 Ma. No vertical exaggeration.

formation. As will be shown in the next sections, the surface uplift is sensitive to a number of parameters. Some previous numerical results [60] predict bi-phase surface uplift, e.g. the first phase produces about 700 m uplift at the centre of the plume and the second phase results in a maximum uplift of 1300 m after 40 Ma. Semi-analytical estimations by Davies [59] predict an initial uplift of 500 m and consequent 1500 m uplift, resulting from erosion of the lithosphere. Previous experiments based on local isostatic assumption [8,54,61,62] find a maximum topographic uplift of about 1300–1350 m.

Our reference model predicts a long-wavelength dynamic surface uplift with amplitude of 1700 m achieved already after the first 0.1 Ma (Fig. 5f). At this moment the plume head is still very deep (at 300–350 km depth). The major long-wavelength elevation event (1600 m) occurs at 0.95 Ma (Fig. 5f). The highest elevations recorded during test simulations are of the order of 1800 m at 1.4 Ma after the start of simulations in the case of an asthenospheric viscosity of  $10^{20}$  Pa s and  $\Delta T = 500^\circ\text{C}$  (Fig. 5c).

#### 4.2.5. Benchmark test using a Newtonian model

We have also tested our model against the previous Newtonian studies [8]. For these tests we used Newtonian rheology for the lithosphere and the crust (Fig. 5b') and assumed local isostasy. The resulting elevation is 1200 m, which is 300 m (25%) higher than in the model of Fig. 5b that accounts for the 'true' lithosphere. Depending on different density and temperature anomalies used for the plume models (Fig. 5a–f), various amplitudes of surface uplift from 600 to 1800 m

can be predicted. Under the assumption of local isostasy the same parameters yield elevations from 900 to 2100 m. Consequently, the lithospheric flexure plays a significant part (30%) in the long-scale reaction of the lithosphere to plume head emplacement.

#### 4.2.6. Lithospheric stress and strain distributions

The predicted stress field provides tectonically important stress distributions in the crust and lithosphere. The shear and normal deviatoric stress fields predict stress localisations on the order of  $\pm 85$ –120 MPa within the first 50 km depth interval that remains effectively elasto-plastic (Fig. 6). The horizontal extensional stress is localised within the elasto-plastic part of the lithosphere above the rising plume. The ascent of the plume results in upward lithospheric flexure which, in turn, causes additional extension and irreversible plastic failure (faulting).

Compressional lithospheric stresses are observed over both edges of the plume head (Fig. 6). There is a moderate propagation of the convective cells right into the lithosphere, but it does not affect more than half of the initial lithospheric thickness.

The shear stress field indicates extension above the rising plume and compression on the edges, within the first 50 km depth (Figs. 3C–6).

## 5. Discussion and conclusions

For the above reason, comparison with the previous Newtonian studies is not simple. The plume behaviour in non-Newtonian embeddings is ex-

tremely sensitive to the effective buoyancy forces, so that small variation in the buoyancy force results in a strong variation in the ascent behaviour. For the same driving force, the ascent occurs at rates faster by orders of magnitude than for a Newtonian fluid. The rheologies employed in the previous studies [4,51,53,54] were mostly only temperature-dependent, and thus only roughly approximated the temperature, stress, strain rate and pressure-dependent rheology of mantle silicates. The elastic and brittle rheological terms were neglected or replaced by pseudoplastic or pseudoelastic terms [21], and the upper surface of the previous models was fixed, not permitting vertical deflections of the lithosphere (e.g. [2,8,16,18,19,29]).

### 5.1. Major effects when accounting for explicit rheology, lithospheric flexure and free upper surface

#### 5.1.1. Plate flexure

The predicted intraplate deviatoric stresses reach 110 MPa and are an order of magnitude higher than the basal shear and normal deviatoric stresses ( $< 10$  Ma). This is a typical effect of stress amplification by flexure [11]. This means that lithospheric flexure, and not simply local isostasy, plays an important part in lithospheric reaction to plume head emplacement. The resulting surface deformation wavelengths are affected by the flexural wavelength and not only by that of the plume head, which can also be seen from Figs. 4 and 5. The estimates of the vertical uplift show 30% lower values than the predictions obtained using local isostasy, which once again indicates the importance of flexural deformation.

#### 5.1.2. Vertical uplift and plate thinning

The predicted amplitudes and histories of surface uplift are different, in a number of details, from previous models: (1) The first elevation event appears in less than 0.3–0.5 Ma after plume initiation. (2) The amplitude of the surface uplift is basically 30% lower than for the local isostatic predictions. (3) Strain rates at the base of the lithosphere are strongly dependent on the viscosity profile through the lithosphere–asthenosphere

transition as well as on the plume–asthenosphere viscosity contrast.

#### 5.1.3. Thermomechanical erosion, rheology, strain localisations and plume ascent rates

Maximum lithospheric erosion and weakening localises in two zones aside the plume head centre. The explanation is three-fold: (1) for a ductile rheology, the contribution from thermal weakening may be less important than that from strain-rate and stress weakening, which are both maximal at the sides of the flattening plume head; (2) lithospheric flexure favours formation of weak zones not only in the middle but also at the sides of a central zone of the utmost flexure [11]; (3) the vertical thinning rate appears to be weakly dependent on the lateral scale of the upwelling, contrary to the geometry and evolution of the area of horizontal thinning, which is dependent on the length of the plume head flattening.

Shear strain localises in narrow bands, which do not exactly follow the lithosphere–asthenosphere boundary, but intrude into the lithosphere (Fig. 3), leading to mechanical decoupling of the competent parts of lithosphere from the underlying ductile substratum composed of both ductilised lithosphere and plume material. Parts of the lithosphere found near the plume head centre are decoupled and rapidly eroded.

Accounting for elasto-plastic terms demonstrates the possibility of spatially alternating stress localisations in the lithosphere.

#### 5.1.4. Ascent rates, plume head emplacement, flattening and lithospheric extension

In our reference experiment, we assumed an initial thermal anomaly of 300°C and a density anomaly of 30 kg/m<sup>3</sup> for the plume (see also [8]). The resulting average velocity of the plume ascent is 1–2 m/yr, allowing the plume to arrive at the bottom of the lithosphere during the first 0.3–0.6 Ma without heat loss, so the plume head has low viscosity when it begins flattening. Consequently, the shear stresses exerted on the bottom of the lithosphere are lower than in the Newtonian models, but the predicted strain rates are one to two orders of magnitude higher, leading to more efficient erosion of the base of the litho-

sphere. Flexural yielding of the lithosphere (Fig. 6) helps the process of mechanical erosion. It may result in 20% thinning [11] of the mechanical plate for plate wavelengths observed in our problem. This is about half the total thinning.

Large-scale lithospheric deformation begins 0.3–0.5 Ma before the onset of plume flattening. It is characterised by basal erosion of the lithosphere and a large-scale upward flexure. The surface elevation recorded on the upper horizontal surface begins at 0.1–0.2 Ma. The plume head is blocked at the base of the lithosphere due to the high strength of the lithospheric layer, and not just because it reaches a neutral buoyancy level. The plume head thus preserves positive buoyancy for a long time after its flattening. The time needed for further thermal weakening of the lithosphere by heat diffusion from the plume is 10–20 to 50 Ma.

Plume head flattening leads to a higher strain around the plume head, resulting in two areas of strong lithospheric thinning with a coefficient of extension from 1.1 to 2 (Figs. 3 and 4). These areas are associated with normal faulting in the surface brittle layer of the lithosphere and nucleate two rifting zones, each located at a horizontal distance of about 600 km from the plume head centre. At later stages, thermal weakening of negatively buoyant lithosphere results in development of negative *RT* instabilities. The central lithospheric zone over the hot plume head undergoes local subsidence due to a negative instability in the heated lithosphere, which is still denser than the plume head.

### 5.2. Plume head emplacement in the Caribbean LIP history

The primary stresses recorded within the lithosphere are due to plate extension above the rising plume (Fig. 6). This prediction matches the primary deformation patterns recorded in the Caribbean LIP, situated in an intraplate geodynamical context. At the opposite side of the volcanic passive continental margins, extension is not usually considered as a boundary condition. In our model, the extensional zone extends over 1000 km for a flattened plume head. The rapid increase of the

geothermal gradient at the base of the lithosphere, associated with plume head emplacement, explains the onset of partial melting of the lithosphere and emplacement of dykes and basaltic flows and the underplating recorded in the CLIP at Turonian time (90–88 Ma) (Fig. 1B). The seaward-dipping reflector sequences observed on the edge of the plateau, in the Venezuelan basin (Fig. 1B), are probably generated by local extension provoked by the predicted return flow cells (Fig. 4) and linked to the deep-seated thermal anomaly, quite similar to a number of other volcanic passive margins (e.g. [63]). Furthermore, large-scale surface uplift with 1000 km wavelength created by the plume dynamics is coeval with the emplacement of the flood basalts and its eastern boundary could be located at the edge of the Venezuelan basin.

We have studied only the first stage of formation of an oceanic LIP. The second logical step of modelling should be focussed on later cooling of the plume head and on the associated late crustal and lithospheric deformations, necessary to go further into the comparison with the CLIP.

### Acknowledgements

The principal authors of the Parovoz code, Y. Podladchikov and A. Poliakov, are deeply thanked for their continuous help in both scientific and even technical matters related to further development of the code. We deeply thank N. Sleep, C. Faccenna, C. Ebinger and C. Farnetani for their thorough and constructive comments. N. Sleep is also thanked for following discussions. C. Jaupart also provided a number of useful comments. This work was supported by CNRS-UMR 7072.[AC]

### References

- [1] W.J. Morgan, Hotspot tracks and the opening of the Atlantic and Indian Oceans, in: C. Emiliani (Ed.), *The Oceanic Lithosphere*, Wiley, New York, 1981, vol. 7, pp. 443–487.
- [2] M. Richards, R.A. Duncan, V.E. Courtillot, Flood basalts and hot-spot tracks: plume heads and tails, *Science* 246 (1989) 103–107.

- [3] I.H. Campbell, R.W. Griffiths, Implications of mantle plume structure for the origin of flood basalts, *Earth Planet. Sci. Lett.* 99 (1990) 79–93.
- [4] R.W. Griffiths, I.H. Campbell, Stirring and structure in mantle plumes, *Earth Planet. Sci. Lett.* 99 (1990) 66–78.
- [5] P. Olson, Hot spots, swells and mantle plumes, in: M.P. Ryan (Ed.), *Magma Transport and Storage*, Wiley, Chichester, 1990, pp. 33–51.
- [6] R.W. Griffiths, Particle motions induced by spherical convective elements in Stokes flow, *J. Fluid Mech.* 166 (1986) 139–159.
- [7] N. Sleep, Lateral flow and ponding of starting plume material, *J. Geophys. Res.* 102 (1997) 10001–10012.
- [8] N.M. Ribe, U.R. Christensen, Three-dimensional modeling of plume-lithosphere interaction, *J. Geophys. Res. B* 99 (1994) 669–682.
- [9] S. Medvedev, Y. Podladchikov, New extended thin-sheet approximation for geodynamic applications; II, Two-dimensional examples, *Geophys. J. Int.* 136 (1999) 586–608.
- [10] J.P. Avouac, E.B. Burov, Erosion as a driving mechanism of intracontinental mountain growth, *J. Geophys. Res.* 101 (1996) 17747–17769.
- [11] E.B. Burov, M. Diament, The effective elastic thickness ( $T_e$ ) of continental lithosphere: What does it really mean?, *J. Geophys. Res. B* 100 (1995) 3905–3927.
- [12] R.S. Huismans, Y. Podladchikov, S. Cloetingh, The transition from passive to active rifting, FEM modeling of convective upwelling of mantle lithosphere beneath rift zones, in: *AGU 1997 Fall Meeting* 78, EOS, Washington, DC, 1997, p. 698.
- [13] E.B. Burov, A.N.B. Poliakov, Erosion and rheology controls on synrift and postrift evolution: Verifying old and new ideas using a fully coupled numerical model, *J. Geophys. Res. B* 106 (2001) 16461–16481.
- [14] R.S. White, D. McKenzie, Mantle plumes and flood basalts, *J. Geophys. Res.* 100 (1995) 17543–17585.
- [15] R.S. White, D.P. McKenzie, Magmatism at rift zones: The generation of volcanic continental margins and flood basalts, *J. Geophys. Res.* 94 (1989) 7685–7729.
- [16] V.S. Solomotov, Grain size-dependent viscosity convection and the thermal evolution of the Earth, *Earth Planet. Sci. Lett.* 191 (2001) 203–212.
- [17] P.J. Tackley, Self-consistent generation of tectonic plates in three-dimensional mantle convection, *Earth Planet. Sci. Lett.* 157 (1998) 9–22.
- [18] P.J. Tackley, Mantle convection and plate tectonics; toward an integrated physical and chemical theory, *Science* 288 (2000) 2002–2007.
- [19] D. Bercovici, Y. Ricard, G. Schubert, A two-phase model for compaction and damage; 3, Applications to shear localization and plate boundary formation, *J. Geophys. Res.* 106 (2001) 8925–8939.
- [20] W.B. Moore, G. Schubert, P.J. Tackley, The role of rheology in lithospheric thinning by mantle plumes, *Geophys. Res. Lett.* 26 (1999) 1073–1076.
- [21] V.S. Solomotov, L.N. Moresi, Scaling of time-dependent stagnant lid convection; application to small-scale convection on Earth and other terrestrial planets, *J. Geophys. Res.* 105 (2000) 21795–21817.
- [22] M.-P. Doin, L. Fleitout, U. Christensen, Mantle convection and stability of depleted and undepleted continental lithosphere, *J. Geophys. Res.* 102 (1997) 2771–2787.
- [23] D.L. Turcotte, G. Schubert, *Applications of Continuum Physics to Geological Problems*, New York, 1982, 450 pp.
- [24] J. Byerlee, Rock friction and earthquake prediction, *Pure Appl. Geophys.* 116 (1978) 615–626.
- [25] G.F. Davies, Temporal variation of the Hawaiian plume flux, *Earth Planet. Sci. Lett.* 113 (1992) 277–286.
- [26] M. Gerbault, A.N.B. Poliakov, M. Daignieres, Prediction of faulting from the theories of elasticity and plasticity; what are the limits?, *J. Struct. Geol.* 20 (1998) 301–320.
- [27] J.P. Morgan, W.J. Morgan, E. Price, Hotspot melting generates both hotspot volcanism and a hotspot swell?, *J. Geophys. Res. B* 100 (1995) 8045–8062.
- [28] W.B. Moore, G. Schubert, Lithospheric thinning and chemical buoyancy beneath the Hawaiian swell, *Geophys. Res. Lett.* 24 (1997) 1287–1290.
- [29] C.G. Farnetani, M.A. Richards, M.S. Ghiorso, Petrological models of magma evolution and deep crustal structure beneath hotspots and flood basalt provinces, *Earth Planet. Sci. Lett.* 143 (1996) 81–94.
- [30] H.W. Cooper, G. Simmons, The effect of cracks on the thermal expansion of rocks, *Earth Planet. Sci. Lett.* 36 (1977) 404–412.
- [31] S.J. Bauer, J. Handin, Thermal expansion and cracking of three confined, water-saturated igneous rocks to 800°C, *Rock Mech. Rock Eng.* 16 (1983) 181–198.
- [32] R.A. Duncan, M.A. Richards, Hotspots, mantle plumes, flood basalts, and true polar wander, *Rev. Geophys.* 29 (1991) 31–50.
- [33] W.B. Moore, G. Schubert, P.J. Tackley, Three-dimensional simulations of plume-lithosphere interaction at the Hawaiian swell, *Science* 279 (1998) 1008–1011.
- [34] J.T. Ratcliff, D. Bercovici, G. Schubert, L.W. Kroenke, Mantle plume heads and the initiation of plate tectonic reorganizations, *Earth Planet. Sci. Lett.* 156 (1998) 195–207.
- [35] J.A. Whitehead, D.S. Luther, Dynamics of laboratory diapir and plume models, *J. Geophys. Res.* 80 (1975) 705–717.
- [36] D.E. Loper, F.D. Stacey, The dynamical and thermal structure of deep mantle plumes, *Phys. Earth Planet. Inter.* 33 (1983) 304–317.
- [37] R.F. Weinberg, Y. Podladchikov, Diapiric ascent of magmas through power law crust and mantle, *J. Geophys. Res.* 99 (1994) 9543–9559.
- [38] A.N.B. Poliakov, P. Cundall, Y. Podladchikov, V. Laykhovsky, An explicit inertial method for the simulation of viscoelastic flow: an evaluation of elastic effect on diapiric flow in two- and three-layers models, in: D. Stone, S.K. Runcorn (Eds.), *Dynamic Modelling and Flow in the Earth and Planets*, Kluwer, Holland, 1993, pp. 175–195.
- [39] P.A. Cundall, Numerical experiments on localization in frictional materials, *Ing. Arch.* 59 (1989) 148–159.

- [40] T.N. Edgar, J.B. Saunders, DSDP Init. Report 15 (1973) 1137.
- [41] H. Sigurdsson, R.M. Leckie, G.D. Acton et al., Proc. ODP Init. Reports 165 (1997) 865.
- [42] J.L. Pindell, S.F. Barrett, Geological evolution of the Caribbean region, in: G. Dengo, J.E. Case (Eds.), *The Geology of North America, the Caribbean Region (A Decade of North American Geology)*, Geological Society of America, Boulder, CO, 1990, vol. H, pp. 405–432.
- [43] J.E. Case, W.D. MacDonald, P.J. Fox, Caribbean crustal provinces; seismic and gravity evidence, in: G. Dengo, J.E. Case (Eds.), *The Geology of North America, the Caribbean Region (A Decade of North American Geology)*, Geological Society of America, Boulder, CO, 1990, vol. H, pp. 15–36.
- [44] A. Mauffret, S. Leroy, Seismic stratigraphy and structure of the Caribbean igneous province, *Tectonophysics* 283 (1997) 61–104.
- [45] N.W. Driscoll, J.D. Diebold, Tectonic and stratigraphic development of the Eastern Caribbean: new constraints from multichannel seismic data, in: P. Mann (Ed.), *Caribbean Sedimentary Basins*, Elsevier, Amsterdam, 1999, pp. 591–626.
- [46] A. Mauffret, S. Leroy, J.M. Vila, E. Hallot, B.M.d. Lépinay, R.A. Duncan, Prolonged magmatic and tectonic development of the Caribbean igneous province revealed by a diving submersible survey, *Mar. Geophys. Res.* 22 (2001) 17–45.
- [47] S. Révillon, N.T. Arndt, E. Hallot, A.C. Kerr, J. Tarney, Petrogenesis of picrites from the Caribbean Plateau and the North Atlantic magmatic province, *Lithos* 49 (1999) 1–21.
- [48] E.B. Burov, S. Cloetingh, Erosion and rift dynamics new thermomechanical aspects of post-rift evolution of extensional basins, *Earth Planet. Sci. Lett.* 150 (1997) 7–26.
- [49] G. Ranalli, *Rheology of the Earth*, London, 1995, 413 pp.
- [50] S.H. Kirby, A.K. Kronenberg, Rheology of the lithosphere: Selected topics, *Rev. Geophys.* 25 (1987) 1219–1244.
- [51] C.G. Farnetani, M.A. Richards, Numerical investigations of the mantle plume initiation model for flood basalt events, *J. Geophys. Res. B* 99 (1994) 13813–13833.
- [52] P. van Keken, Evolution of starting mantle plumes: a comparison between numerical and laboratory models, *Earth Planet. Sci. Lett.* 148 (1997) 1–11.
- [53] A.M. Leitch, G.F. Davies, Mantle plumes and flood basalts: Enhanced melting from plume ascent and an eclogite component, *J. Geophys. Res. B* 106 (2001) 2047–2059.
- [54] A. Manglik, N.I. Christensen, Effect of mantle depletion buoyancy on plume flow and melting beneath a stationary plate, *J. Geophys. Res.* 102 (1997) 5019–5028.
- [55] J.F. Allan, T. Simkin, Fernandina volcano's evolved, well-mixed basalts: Mineralogical and petrological constraints on the nature of the Galapagos plume, *J. Geophys. Res. B* 105 (2000) 6017–6041.
- [56] P.R. Stoddard, On the relations between transform zones resistance and plate motion, *J. Geophys. Res.* 97 (1992) 17637–17650.
- [57] E. Burov, C. Jaupart, L. Guillou-Frottier, Ascent and emplacement of magma reservoirs in brittle-ductile upper crust, *J. Geophys. Res.* (2002) submitted.
- [58] P. Olson, G. Schubert, C. Anderson, P. Goldman, Plume formation and lithospheric erosion: A comparison of laboratory and numerical experiments, *J. Geophys. Res.* 93 (1988) 15065–15084.
- [59] G.F. Davies, Thermomechanical erosion of the lithosphere by mantle plumes, *J. Geophys. Res.* 99 (1994) 15709–15722.
- [60] M. Monnereau, M. Rabinowicz, E. Arquís, Mechanical erosion and reheating of the lithosphere: a numerical model for hotspot swells, *J. Geophys. Res. B* 98 (1993) 809–823.
- [61] N.M. Ribe, U.R. Christensen, The dynamical origin of Hawaiian volcanism, *Earth Planet. Sci. Lett.* 171 (1999) 517–531.
- [62] L. Cserepes, U.R. Christensen, N.M. Ribe, Geoid height versus topography for a plume model of the Hawaiian swell, *Earth Planet. Sci. Lett.* 178 (2000) 29–38.
- [63] L. Geoffroy, J.P. Callot, S. Scaillet, A. Skuce, J.P. Gélard, M. Ravilly, J. Angelier, B. Bonin, C. Cayet, K. Perrot, C. Lepvrier, Southeast Baffin volcanic margin and the North American-Greenland plate separation, *Tectonics* 20 (2001) 566–584.
- [64] N.L. Carter, M.C. Tsenn, Flow properties of continental lithosphere, *Tectonophysics* 36 (1987) 27–63.